# Relationship Analysis of PM$_{2.5}$ and BLH using Aerosol and Turbulence Detection Lidar

Chong Wang[1,2,*], Mingjiao Jia[2,*], Haiyun Xia[1,2], Yunbin Wu[1], Tianwen Wei[1], Xiang Shang[1], Chengyun Yang[1], Xianghui Xue[1,2], Xiankang Dou[1,3]

[1]CAS Key Laboratory of Geospace Environment, University of Science and Technology of China, Hefei, 230026, China
[2]Glory China Quantum Lidar Co. Ltd., Shanghai, 201315, China
[3]School of Electronic Information, Wuhan University, Wuhan, 430072, China
[*]These authors contributed equally to this work.

*Correspondence to*: Haiyun Xia (hsia@ustc.edu.cn)

**Abstract.** The atmospheric boundary layer height (BLH) is a key parameter in weather forecast and air quality prediction. To investigate the relationship between BLH and air pollution under different conditions, a compact micro-pulse lidar integrated both direct detection lidar (DDL) and coherent Doppler wind lidar (CDWL) is built. Then the BLH can be determined from aerosol density or vertical wind independently. During a 45-hour continuous observation in June 2018, stable boundary layer, residual layer and convective boundary layer are identified. Fine structure of aerosol layers, drizzles and vertical wind near cloudbase are also detected. In comparison, the standard deviation between BLH values derived from DDL and CDWL is 60 m, indicating the accuracy of this work. The retrieved convective BLH is a little higher than that from ERA5 reanalysis due to different retrieval methods. Negative correlation between BLH and PM$_{2.5}$ is analyzed before and after a precipitation. A criterion is proposed to classify the residual layer and convective boundary layer. Different trends show that the relationship between PM$_{2.5}$ and BLH should be considered in different boundary layer categories.

## 1 Introduction

In recent decades, with rapid urbanization, air pollution has become a severe environmental problem in China (Song et al., 2017; Li et al., 2016; Chan and Yao, 2008; Zhang et al., 2012). Particulate matter (PM) with aerodynamic diameter less than 2.5 μm (PM$_{2.5}$), attracts public attentions due to its adverse effects on human health and environment (Brunekreef and Holgate, 2002; Kampa and Castanas, 2008; Huang et al., 2014; Cohen et al., 2017). In addition to pollutant emissions and topographic conditions, the spatial and temporal distribution of PM is mainly affected by meteorological conditions in troposphere, especially in atmospheric boundary layer (ABL) (Chen et al., 2018; Wei et al., 2018; Song et al., 2017; Li et al., 2017b; Su et al., 2018).

The ABL, also called PBL (planetary boundary layer), plays an important role in lower troposphere. ABL is directly influenced by and responds to the Earth's surface activities, such as frictional drag, evaporation, transpiration and heat transfer, with a timescale of an hour or less (Stull, 1988). The ABL consists of three major parts during the diurnal evolution:

convective boundary layer (CBL), stable boundary layer (SBL) and residual layer (RL) (Stull, 1988). The ABL is a key factor in control and management of air quality, numerical weather prediction, urban and agricultural meteorology, aeronautical meteorology, hydrology and so on (Large et al., 1994). The boundary layer height (BLH) is the height of the top layer of ABL, above which is the free atmosphere. Pollutants or any constituents within this layer is fully mixed and

5    vertically dispersed due to convection or mechanical turbulence (Seibert, 2000). The BLH determines the volume available for pollution dispersion and transport in the atmosphere. Low BLH and weak turbulence strengthen the accumulation of air pollutants (Petaja et al., 2016; Miao et al., 2018). Hence, the BLH is one of the fundamental parameters in dispersion models. A roughly anti-correlation relationship between $PM_{2.5}$ and BLH have been found in recent years (Du et al., 2013; Petaja et al., 2016; Miao et al., 2018; Su et al., 2018). However, the relationship analysis of $PM_{2.5}$ and BLH in different ABL categories is

10   still rare. Therefore, continuous observation of the BLH with high temporal and spatial resolution and the relationship between pollutions and BLH is desirable for air quality prediction.

There are always significant changes in vertical profiles of aerosol concentration, specific humidity, potential temperature or turbulence around the top layer of ABL, making it possible to derive the BLH. There are several instruments used for the determination of BLH based on the sharp gradient in the vertical profiles mentioned above (Seibert, 2000; Baars et al., 2008;

15   Li et al., 2017a; Yang et al., 2017; Bonin et al., 2018). For example, in-situ instruments, such as radiosonde, balloon, mast and aircraft, and remote sensing instruments, such as sodar, wind profiler, lidar and ceilometer. All of these instruments have advantages and shortcomings regarding accuracy, detection range, spatial and temporal resolution as summarized by Seibert (2000). Among these instruments, lidar provides sufficient spatial and temporal resolution, long detection range and high accuracy to determine the BLH. These qualities make lidar a powerful tool for BLH assessment.

20   In recent decades, lidars are widely used in lower atmosphere via Mie scattering, Raman scattering and differential absorption (Godin et al., 1989; Campbell et al., 2002; Renaut et al., 1980; Murray and van der Laan, 1978; Xia et al., 2007; Reitebuch, 2012), in middle atmosphere via Rayleigh scattering (Xia et al., 2012; Xia et al., 2014; Dou et al., 2009; Lux et al., 2018), in mesosphere and lower thermosphere via fluorescence backscatter (She et al., 1992; Gao et al., 2015; Li et al., 2018; Qiu et al., 2016). Aerosol, trace gas concentration, atmospheric density and temperature, wind, and neutral metal atom

25   can be detected by these lidars. Recently, a micro-pulse direct detection lidar (DDL) was developed to make continuous measurements of aerosol in troposphere (Xia et al., 2015). A coherent detection Doppler wind lidar (CDWL) was developed to measure wind field in ABL (Wang et al., 2017). Based on these two lidars, BLH values can be derived from both aerosol density and turbulence. The simultaneous implementation of DDL and CDWL will improve the precision of BLH assessment and enrich the meteorological data in ABL.

30   Generally, DDL and CDWL belong to different lidar categories. In this work, a hybrid lidar integrating both systems are developed for simultaneous measurements of aerosol and vertical wind. The integrated lidar is utilized to further understand the relationship between $PM_{2.5}$ and BLH. The integrated lidar system, meteorology and PM data are described in Sect. 2. The retrieval methods of BLH are briefly introduced in Sect. 3. In Sect. 4, the results and discussions on lidar data, the retrieved BLH and the relationship between $PM_{2.5}$ and BLH are presented. Finally, the conclusion and summary are drawn in Sect. 5.

## 2 Instruments and Data

### 2.1 The integrated lidar system

A compact and integrated micro-pulse lidar system is developed. Benefiting from all-fiber configuration and up-conversion technology, the lidar inherits advantages from both DDL and CDWL. The DDL is based on up-conversion technology and is

5  used for long-range aerosol measurement (Xia et al., 2015). The CDWL is used for wind field measurement (Wang et al., 2017). Two lidar systems use only one set of laser source, optical collimator and control system. The unique optical telescope guarantees that the measured signal in both systems are from the same backscattering volume, and the radial wind profile and aerosol concentration are measured simultaneously.

The diagram of the system is shown in Fig. 1. The seed laser emits continues wave (CW) at 1548 nm, then the CW is split

10  into local oscillator and transmitted seed laser by a beam splitter (BS). The transmitted seed laser is chopped, and frequency shifted 80 MHz by an acoustic-optical modulator (AOM). After the AOM, the transmitted laser is amplified by an Erbium doped fiber amplifier (EDFA) and transmitted into the atmosphere via a collimator. The pulse duration is 300 ns and the pulse energy is 110 µJ. The atmospheric backscattering is collected by two telescopes, adopting double 'D' configuration. As shown in Fig. 1, the two aspheric lenses are glued together with parallel optical axes for easy alignment and avoiding blind

15  zone. The absolute overlap distance is 1 km. On the CDWL channel, the backscattering pass through a circulator is chopped by an optical switch (OS), which cuts off the reflection light from the circulator and lens. The reflection light is much higher than the atmospheric backscattering and will cause saturation and even breakdown in the balanced detector (BD). After the OS, the backscattering is mixed with local oscillator and measured on the BD. The analog signal is converted to digital signal by an ADC and then processed by a PC. On the DDL channel, the backscattering is collected and mixed with a pump

20  laser at 1950 nm in a wavelength division multiplexer (WDM). The mixed laser then passes through the periodically poled lithium niobate waveguide (PPLN). The backscattering at 1548 nm is converted to 863 nm by the PPLN and detected by a Silicon single-photon detector (SPD). A filter is used to filter out the noise. A multi-channel scaler (MCS) records the digital signal. Benefiting from coherent detection and the narrow passband of the PPLN, this integrated lidar can perform all-day detection of the atmosphere. The detailed parameters of the integrated lidar are listed in the Table 1.

25  During the experiment, the integrated lidar is pointed vertically. Then the vertical wind and backscattering intensity are measured simultaneously. The raw DDL data is recorded with a spatial and temporal interval of 45 m and 2 s, respectively, while CDWL data is 60 m and 2 s, respectively. The integrated lidar is deployed 5 m above ground on the campus of University of Science and Technology of China (USTC, 117.26 °E, 31.84 °N), an urban area in Hefei, China.

### 2.2 Meteorology and PM$_{2.5}$ data

30  A weather transmitter (Vaisala WXT520) is used to measure meteorological parameters, including temperature, relative humidity, barometric pressure, wind velocity and direction. A visibility sensor (Vaisala PWD50) is used to measure the atmospheric visibility. A wide range aerosol spectrometer (Grimm Mini WRAS 1371) measures aerosol volume size

distribution ranging from 10 nm to 35 μm over 41 channels (Shang et al., 2018). Then $PM_{2.5}$ and $PM_{10}$ values are calculated. All these instruments were deployed 60 m above ground and 250 m east of the integrated lidar on the top of a research building in USTC. During the experiment, all these meteorological data are recorded with an interval of 1min.

## 3 BLH retrieval methods

5 The BLH is retrieved from both aerosol concentration and vertical wind in this experiment. For the DDL data, the range corrected lidar signal (RCS), $N(R)R^2$, has a sharp decrease at BLH, where $N(R)$ is the backscattering photon number from altitude of R. As for the CDWL, the temporal vertical velocity variation in the ABL is much stronger than that in the free atmosphere. The carrier to noise ratio (CNR) of the CDWL also represents the aerosol concentration, which can also be used to determine the BLH.

10 Haar wavelet covariance transform (HWCT) method is used to retrieve BLH from aerosol concentration. The HWCT $W_f(a, b)$ is defined as (Brooks, 2003):

$$W_f(a, b) = \frac{1}{a} \int_{z_b}^{z_t} f(z)\, h\left(\frac{z - b}{a}\right) dz \quad , \tag{1}$$

with the Haar function:

$$h\left(\frac{z - b}{a}\right) = \begin{cases} 1, b - \dfrac{a}{2} \leq z \leq b \\ -1, b \leq z \leq b + \dfrac{a}{2} \\ 0, elsewhere \end{cases} \tag{2}$$

Where $f(z)$ is the normalized RCS or CNR, $z_b$ and $z_t$ are the bottom and top height of a selected range, a is the dilation of the Haar wavelet and b is the center position of the Haar function. For a given dilation, the height where maximum $W_f(a, b)$

15 appears is considered to be the BLH. Considering different vertical spatial resolutions, a dilation of 150 m and 250 m is applied for RCS and CNR, respectively. Compared with gradient method, HWCT method has greater adjustability and robustness (Korhonen et al., 2014). In order to reduce the interference from unexpected turbulence and noise, the signal is averaged to a temporal resolution of 1 min in BLH determination. As described in Sect. 2.1, RCS should be corrected with an overlap factor before the analysis. As an example, the measured RCS and CNR after one-minute average (after overlap

20 correction and background noise deduction) at 1 June 2018, 10:40 am is shown in Fig. 2a. The corresponding HWCT results are shown in Fig. 2b, from which the BLH can be determined.

The BLH can also be determined from the variance of vertical velocity $\sigma_w^2$, which represented the turbulence kinetic energy. For a given time window and a reliable threshold, below the BLH, the $\sigma_w^2$ is larger than the threshold, and vice versa. The threshold varies from different locations (Huang et al., 2016). In this study, the threshold is set to be 0.06 $m^2s^{-2}$. A median

25 algorithm is used to mitigate the interference and fluctuation from unexpected turbulence and noise. Step (1), select all the

height with $\sigma_w^2$ less than the threshold; Step (2), find the median height $z_m$ selected in Step (1); Step (3), the BLH is the maximum height below $z_m$ that $\sigma_w^2$ larger than the threshold. An example of employing this threshold and algorithm is shown in Fig. 2c. Some confusing points, such as that at ~1.0 km and ~1.6 km in Fig. 2c can be distinguished.

BLH from reanalysis data is always used in boundary layer climatology. ERA5 is the newest generation of ECMWF
5 (European Centre for Medium-Range Weather Forecasts) atmospheric reanalysis of the global climate. ERA5 reanalysis assimilates a variety of observations and models in 4-dimensional. The data has 137 levels from the surface up to 80 km altitude, the horizontal resolution is 0.3 ° for both longitude and latitude (Hersbach and Dee, 2016). The hourly BLH from high resolution realisation sub-daily deterministic forecasts of ERA5 is used here. The BLH in ERA5 is determined by the bulk Richardson number ($Ri_b$) method (ECMWF, 2017; Seidel et al., 2012; Vogelezang and Holtslag, 1996). The bulk
10 Richardson number $Ri_b$ is defined as (Vogelezang and Holtslag, 1996):

$$Ri_b = \frac{gh(\theta_{vh} - \theta_{v0})}{\theta_{v0}(u_h^2 + v_h^2)} \quad . \tag{3}$$

Here $g$ is the acceleration of gravity, $h$ is height, $\theta_{v0}$ and $\theta_{vh}$ are the virtual potential temperature at the surface and $h$, $u_h$ and $v_h$ are component wind speeds at h, respectively. The BLH is then defined as the lowest height where the $Ri_b$ reaches a critical value of 0.25 (ECMWF, 2017).

## 4 Results and discussion

15 ### 4.1 Observational results

Figure 3 shows a continuous observation over 45 hours from 1 June to 2 June in 2018. The RCS with 1 min temporal resolution, CNR and vertical wind with 20 s temporal resolution are shown, respectively. The black dotted line in each panel indicated the BLH derived from RCS, CNR and vertical wind. The BLH results are defined as BLH$_\text{RCS}$, BLH$_\text{CNR}$ and BLH$_\text{VAR}$ in this study. Sunrise and sunset times at local time (LT) of 05:06 and 19:12 are marked by red triangles and blue
20 inverted triangles. The experimental observation ends with rainfall at ~2 June, 21:00 LT.

As shown in Fig. 3a, aerosol layer experiences a significant diurnal cycle within a height of 2 km. Before 1 June, 09:00 LT, a SBL caused by radiative cooling from the ground can be easily found below ~0.7 km with higher aerosol concentration than that in the RL. Subsequently, the ABL starts to grow due to solar heating after sunrise and deepens to a maximum height of about 2km in mid-afternoon. Stratocumulus appears at the top of the ABL with strong backscattering signal. During the night
25 from 1 June, 22:00 to 2 June, 06:00, the backscattering increases in the RL, which is related to the increase of aerosol concentration. After the sunrise on June 2, the ABL grows as it on June 1, but the BLH is lower than that on June 1.

The CNR measured by CDWL is shown in Fig. 3b. The evolution of ABL is similar to that of RCS. The results observed in RCS can be also found in CNR. Figure 3c shows the height-time cross section of vertical wind. To guarantee the precision of the wind measurements, the data with CNR below -35 dB is abandoned (Wang et al., 2017). The downward vertical wind is

positive and vice versa. Obviously, the convective ABL is well mixed with strong turbulence during the daytime between sunrise and sunset. Wave-like motions also exist in the nocturnal ABL associated with stratified atmosphere.

Cloud with strong backscattering can be detected between ~3 and ~9 km height by both DDL and CDWL. Corresponding vertical velocity of cloud is measured by the CDWL. Fine cloud structures above the ABL are shown in RCS with high

5   spatial and temporal resolution due to higher detection efficiency. In addition, in the height ranging from ~3 to ~6 km on June 1, several transport aerosol layers can be detected in RCS despite accompanying sunshine induced noise. Interestingly, the transport aerosol layers meet the cloudbase during the night on June 1. The fine structures around cloudbase suggest the existence of drizzles. Moreover, precipitation in cloud can be identified by assuming that precipitation has a fall velocity greater than 1 m s$^{-1}$ (Manninen et al., 2018). A precipitation case is indicated by the red arrow in Fig. 3c at approximately 2

10  June, 02:00 LT. The PM$_{2.5}$ value measured simultaneously is illustrated as the brown dotted line in Fig. 3c. A sharp increase of PM$_{2.5}$ occurs during the precipitation. These results hint the potential applications of this integrated lidar in the investigations of aerosol-cloud-precipitation interactions.

The simultaneous measurements of meteorological parameters including temperature, pressure, wind velocity, wind direction, visibility and relative humidity near the ground are shown in Fig. 4a to c. Weak wind condition (velocity less than

15  4 m s$^{-1}$) during the whole experiment is not conducive to the aerosol diffusion near the ground. The wind direction is always northly despite the easterly wind before sunrise on June 1. Two haze event occurred, with visibility less than 10 km and relative humidity less than 80%, during this experiment (Administration, 2010). As mentioned before, there is a sudden increase in PM$_{2.5}$ at approximately 2 June, 02:00 LT during the precipitation. There are also sudden changes in relative humidity and visibility at the same time indicated by the vertical dash-dotted lines. Simultaneous measurements of aerosol

20  size volume distribution during this experiment is shown in Fig. 4d. The amount of aerosol rises in all size channels at ~2 June, 02:00 LT. Concentrations of PM$_{2.5}$ and PM$_{10}$ have almost the same evolution processes. It reveals that there is no specified anthropogenic emissions. Therefore, the experiment is chopped into two sections by the precipitation, as the vertical dash-dotted lines in Fig. 4.

## 4.2 BLH retrieval results

25  As shown in Fig. 3, the BLH results are well retrieved, indicating that the HWCT and variance methods are appropriate for BLH determination. A comparison is performed as shown in Fig. 5a with retrieved BLH$_{RCS}$, BLH$_{CNR}$, BLH$_{VAR}$ and BLH from ERA5 (BLH$_{ERA5}$). Noted that the BLH$_{RCS}$ and BLH$_{CNR}$ are smoothed with median value by a 5 min temporal window. The BLH$_{VAR}$ is smoothed by a 20 min temporal window. In general, there is a significant diurnal variation in BLH as expected. In turbulence derived CBL, all three BLH results from lidar measurements are comparable when the ABL is fully

30  mixed. While in nocturnal ABL, the BLH$_{RCS}$ and BLH$_{CNR}$ are much higher than BLH$_{VAR}$ due to residual aerosol and weak turbulence in RL. Therefore, a criteria is proposed to classify the ABL as CBL and RL/SBL by the values of BLH$_{VAR}$ and BLH$_{RCS}$ in this study. In the evening, a SBL is capped by a RL as shown in Fig. 5a. In the morning, when BLH$_{VAR}$ meets the

value of $BLH_{RCS}$, the type of ABL changes from RL/SBL into CBL. In the Afternoon, when $BLH_{VAR}$ departs from $BLH_{RCS}$, the ABL turns into RL/SBL again. This evolution of ABL diurnal cycle is similar to that described in Stull (1988) and Collaud Coen et al. (2014). During the RL/SBL, The SBL and RL are classified by the $BLH_{RCS}$ and $BLH_{VAR}$. For the CBL, the BLH from lidar is a little higher than $BLH_{ERA5}$, especially during afternoon. This is in agreement with earlier analysis that climatological BLH based on Richardson's method is substantially lower than BLH derived from other methods (Seidel et al., 2010). While for the SBL, the $BLH_{VAR}$ is comparable with $BLH_{ERA5}$.

For a quantitative analysis, statistical comparisons of $BLH_{RCS}$ with $BLH_{VAR}$ and $BLH_{CNR}$ are visualized in Fig. 5b and c. The $BLH_{VAR}$ and $BLH_{CNR}$ are plotted versus the corresponding $BLH_{RCS}$. Scatter diagrams of data points almost lie on the blue and red dashed lines that represent $BLH_{VAR} = BLH_{RCS}$ and $BLH_{CNR} = BLH_{RCS}$, respectively. Note that the $BLH_{RCS}$ is interpolated to the same time series of $BLH_{VAR}$ in Fig. 5b and only BLH in CBL is plotted. The $BLH_{CNR}$ agrees well with $BLH_{RCS}$, despite a difference in RL in the early morning on June 2. The differences between the two results show a standard deviation of 0.06 km of the Gauss fitting. For the CBL, the $BLH_{VAR}$ also agrees well with $BLH_{RCS}$, with a standard deviation of 0.17 km through Gauss fitting.

## 4.3 Relationship between PM₂.₅ and BLH

Recently, Su et al. (2018) and Miao et al. (2018) investigated the relationships between the BLH and surface pollutants in China. The influences of topography, seasonal variation, emissions and meteorological conditions on the BLH-PM₂.₅ relationship were discussed. Nevertheless, due to the relatively low temporal resolution from space-borne lidar and radiosonde measurements, the influence of different ABL types on the BLH-PM₂.₅ relationship are rarely studied.

Figure 5d and e show the relationships between PM₂.₅ concentration and BLH. The correlation coefficients between BLH ($BLH_{RCS}$ in CBL and RL, and $BLH_{VAR}$ in CBL) and PM₂.₅ before and after precipitation in Fig. 5d and e are listed in Table 2. An obvious anti-correlation is shown before precipitation between BLH and PM₂.₅ concentrations in both CBL and RL with correlation coefficient of ~ -0.9. An inverse fitting formula $PM_{2.5}=A+B/BLH$ is used to describe the PM₂.₅-BLH relationships in Fig. 5d. The resulted parameters of $A$, $B$ are listed in Table 2. The nonlinear inverse function shows good performance with coefficient of determination $R^2$=0.84, 0.65 and 0.85. In general, these results show good responses of PM₂.₅ to aerosol derived BLH evolution with larger $R^2$ than turbulence derived BLH before precipitation. In addition, as shown in Fig. 5d, the inverse function of PM₂.₅ to the $BLH_{RCS}$ and $BLH_{VAR}$ show good consistency in CBL. While in RL, the inverse function of PM₂.₅ to the $BLH_{RCS}$ is quite different from that in CBL. The parameter $A$ in the inverse fitting formula of the PM₂.₅-BLH relationship for $BLH_{RCS}$ in RL is triple/twice as large as that for $BLH_{RCS}/BLH_{VAR}$ in CBL as listed in Table 2, while the parameter $B$ has similar values. This difference of parameter $A$ represents a higher PM₂.₅ concentration in RL. After precipitation, as shown in Fig. 5e and Table 2, there are relatively weak anti-correlations of -0.34, -0.21 and -0.22, respectively. Therefore, the relationships between BLH and PM2.5 are affected by unknown aerosol sources after precipitation. Therefore, BLH in different ABL categories, pollutant and weather conditions should be considered in air quality prediction models.

## 4.4 Aerosol-Cloud-ABL interaction

Moreover, the ABL in cloudy condition on June 2 grows slower with lower BLH than that in fair weather on June 1 as shown in Fig. 5a. The maximum BLH on June 2 is about 1.7 km high while the maximum BLH on June 1 is about 2.3 km high. This may be in relation to the aerosol-cloud-ABL interaction. There are several transport aerosol layers above ABL as shown in Fig. 3a. These transport aerosol layers may act as the cloud condensation nuclei during the cloud formation between ~3 and ~5 km on June 2. The clouds play important roles in earth's energy budget. As more incoming solar radiation is reflected and absorbed by clouds, less energy enters the ABL, resulted in weaker CBL development and lower BLH on June 2 than that on June 1. In addition, the weaker convection may lead to the higher aerosol concentration in ABL on June 2 as shown in Fig. 3a and 3(b). These results hinted a strong aerosol-cloud-ABL interaction during the ABL evolution.

## 5 Conclusion

A compact integrated lidar system that integrates both DDL and CDWL is demonstrated. This integrated lidar can make simultaneous measurements of aerosol density, vertical wind and clouds with high spatial and temporal resolution.

The BLH values derived from aerosol and turbulence are determined from 45-hour continuous measurements. Two methods of HWCT and variance are employed in BLH determination, respectively. The daytime CBL can be recognized by both aerosol and vertical wind measurements. The nocturnal RL can be derived from the aerosol density while nocturnal SBL can be derived from vertical wind measurements. The standard deviation between aerosol derived BLH from DDL and CDWL is 0.06 km. The BLH derived from vertical wind is comparable with BLH from ERA5 reanalysis data, also with larger BLH than ERA5 due to different retrieval methods as in other studies (Seidel et al., 2010). During the evolution of ABL, the clouds suppress the growth of ABL, leading aerosol increase in ABL. The relationships between $PM_{2.5}$ and BLH in different ABL categories adopting different methods are analyzed. There is a strong inverse relation between BLH and $PM_{2.5}$ in both CBL and RL before a precipitation. However, the relationship is relative weak after the precipitation.

The reasons for the differences in the relationships between BLH and $PM_{2.5}$ under different pollutant and weather conditions need further studies. This required more data based on different instruments, such as horizontal wind field (Shangguan et al., 2017), temperature profiles (Mattis et al., 2002), and depolarization ratio of aerosol (Qiu et al., 2017) in ABL. The application of such an integrated lidar in this research will contribute to our understanding of ABL and aerosol-cloud-precipitation interactions. Thus improve our ability in weather forecast and air quality prediction in future.

*Data availability*

The ERA5 data sets are publicly available from ECMWF website at https://www.ecmwf.int/en/forecasts/datasets/reanalysis-datasets/era5. Lidar and meteorological data can be downloaded from http://www.lidar.cn/datashare/Wang_et_al_2018c.rar.

*Author contribution*

HX and XD conceived and designed the study. CW, YW, TW performed the lidar experiments observations. XS performed the meteorological and PM observations. CY downloaded and analyzed ERA5 data. MJ and CW carried out the data analysis and prepared the figures, with comments from other co-authors. CW, MJ, HX and XX interpreted the data. CW, MJ and HX wrote the manuscript. All authors contributed to discussion and interpretation.

*Competing interests.*

The authors declare that they have no conflict of interest.

*Acknowledgements.*

We acknowledge the use of ERA5 data sets from ECMWF website at https://www.ecmwf.int/en/forecasts/datasets/reanalysis-datasets/era5. We are grateful to Shengfu Lin, Mingjia Shangguan and Jiawei Qiu for valuable discussions.

## References

Administration, C. M.: Observation and forecasting levels of haze, QX/T 113-2010, China Meteorological Press, Beijing, China, 8, http://www.cma.gov.cn/root7/auto13139/201612/t20161213_350244.html, 2010.

Baars, H., Ansmann, A., Engelmann, R., and Althausen, D.: Continuous monitoring of the boundary-layer top with lidar, Atmospheric Chemistry and Physics, 8, 7281-7296, 10.5194/acp-8-7281-2008, 2008.

Bonin, T. A., Carroll, B. J., Hardesty, R. M., Brewer, W. A., Hajny, K., Salmon, O. E., and Shepson, P. B.: Doppler Lidar Observations of the Mixing Height in Indianapolis Using an Automated Composite Fuzzy Logic Approach, Journal of Atmospheric and Oceanic Technology, 35, 473-490, 10.1175/jtech-d-17-0159.1, 2018.

Brooks, I. M.: Finding Boundary Layer Top: Application of a Wavelet Covariance Transform to Lidar Backscatter Profiles, Journal of Atmospheric and Oceanic Technology, 20, 1092-1105, 10.1175/1520-0426(2003)020<1092:fbltao>2.0.co;2, 2003.

Brunekreef, B., and Holgate, S. T.: Air pollution and health, The Lancet, 360, 1233-1242, 10.1016/s0140-6736(02)11274-8, 2002.

Campbell, J. R., Hlavka, D. L., Welton, E. J., Flynn, C. J., Turner, D. D., Spinhirne, J. D., Scott, V. S., and Hwang, I. H.: Full-Time, Eye-Safe Cloud and Aerosol Lidar Observation at Atmospheric Radiation Measurement Program Sites: Instruments and Data Processing, Journal of Atmospheric and Oceanic Technology, 19, 431-442, 10.1175/1520-0426(2002)019<0431:ftesca>2.0.co;2, 2002.

Chan, C. K., and Yao, X.: Air pollution in mega cities in China, Atmospheric Environment, 42, 1-42, 10.1016/j.atmosenv.2007.09.003, 2008.

Chen, Y., An, J. L., Sun, Y. L., Wang, X. Q., Qu, Y., Zhang, J. W., Wang, Z. F., and Duan, J.: Nocturnal Low-level Winds and Their Impacts on Particulate Matter over the Beijing Area, Advances in Atmospheric Sciences, 35, 1455-1468, 10.1007/s00376-018-8022-9, 2018.

Cohen, A. J., Brauer, M., Burnett, R., Anderson, H. R., Frostad, J., Estep, K., Balakrishnan, K., Brunekreef, B., Dandona, L., Dandona, R., Feigin, V., Freedman, G., Hubbell, B., Jobling, A., Kan, H., Knibbs, L., Liu, Y., Martin, R., Morawska, L., Pope, C. A., Shin, H., Straif, K., Shaddick, G., Thomas, M., van Dingenen, R., van Donkelaar, A., Vos, T., Murray, C. J. L., and Forouzanfar, M. H.: Estimates and 25-year trends of the global burden of disease attributable to ambient air pollution: an analysis of data from the Global Burden of Diseases Study 2015, The Lancet, 389, 1907-1918, 10.1016/s0140-6736(17)30505-6, 2017.

Collaud Coen, M., Praz, C., Haefele, A., Ruffieux, D., Kaufmann, P., and Calpini, B.: Determination and climatology of the planetary boundary layer height above the Swiss plateau by in situ and remote sensing measurements as well as by the COSMO-2 model, Atmospheric Chemistry and Physics, 14, 13205-13221, 10.5194/acp-14-13205-2014, 2014.

Dou, X. K., Li, T., Xu, J. Y., Liu, H. L., Xue, X. H., Wang, S., Leblanc, T., McDermid, I. S., Hauchecorne, A., Keckhut, P., Bencherif, H., Heinselman, C., Steinbrecht, W., Mlynczak, M. G., and Russell, J. M.: Seasonal oscillations of middle atmosphere temperature observed by Rayleigh lidars and their comparisons with TIMED/SABER observations, J Geophys Res-Atmos, 114, 11, 10.1029/2008jd011654, 2009.

Du, C., Liu, S., Yu, X., Li, X., Chen, C., Peng, Y., Dong, Y., Dong, Z., and Wang, F.: Urban Boundary Layer Height Characteristics and Relationship with Particulate Matter Mass Concentrations in Xi'an, Central China, Aerosol and Air Quality Research, 13, 1598-1607, 10.4209/aaqr.2012.10.0274, 2013.

ECMWF: PART IV: PHYSICAL PROCESSES, in: IFS Documentation CY43R3, IFS Documentation, ECMWF, Shinfield Park, Reading, RG2 9AX, England, 221, 2017.

Gao, Q., Chu, X., Xue, X., Dou, X., Chen, T., and Chen, J.: Lidar observations of thermospheric Na layers up to 170 km with a descending tidal phase at Lijiang (26.7°N, 100.0°E), China, Journal of Geophysical Research: Space Physics, 120, 9213-9220, 10.1002/2015ja021808, 2015.

Godin, S., Mégie, G., and Pelon, J.: Systematic lidar measurements of the stratospheric ozone vertical distribution, Geophysical Research Letters, 16, 547-550, 10.1029/GL016i006p00547, 1989.

Hersbach, H., and Dee, D.: ERA5 reanalysis is in production, Shinfield Park, Reading, Berkshire RG2 9AX, UK, 7, 2016.

Huang, M., Gao, Z., Miao, S., Chen, F., LeMone, M. A., Li, J., Hu, F., and Wang, L.: Estimate of Boundary-Layer Depth Over Beijing, China, Using Doppler Lidar Data During SURF-2015, Boundary-Layer Meteorology, 162, 503-522, 10.1007/s10546-016-0205-2, 2016.

Huang, R. J., Zhang, Y., Bozzetti, C., Ho, K. F., Cao, J. J., Han, Y., Daellenbach, K. R., Slowik, J. G., Platt, S. M., Canonaco, F., Zotter, P., Wolf, R., Pieber, S. M., Bruns, E. A., Crippa, M., Ciarelli, G., Piazzalunga, A., Schwikowski, M., Abbaszade, G., Schnelle-Kreis, J., Zimmermann, R., An, Z., Szidat, S., Baltensperger, U., El Haddad, I., and Prevot, A. S.: High secondary aerosol contribution to particulate pollution during haze events in China, Nature, 514, 218-222, 10.1038/nature13774, 2014.

Kampa, M., and Castanas, E.: Human health effects of air pollution, Environmental pollution, 151, 362-367, 10.1016/j.envpol.2007.06.012, 2008.

Korhonen, K., Giannakaki, E., Mielonen, T., Pfüller, A., Laakso, L., Vakkari, V., Baars, H., Engelmann, R., Beukes, J. P., Van Zyl, P. G., Ramandh, A., Ntsangwane, L., Josipovic, M., Tiitta, P., Fourie, G., Ngwana, I., Chiloane, K., and Komppula, M.: Atmospheric boundary layer top height in South Africa: measurements with lidar and radiosonde compared to three atmospheric models, Atmospheric Chemistry and Physics, 14, 4263-4278, 10.5194/acp-14-4263-2014, 2014.

Large, W. G., Mcwilliams, J. C., and Doney, S. C.: Oceanic Vertical Mixing - a Review and a Model with a Nonlocal Boundary-Layer Parameterization, Reviews of Geophysics, 32, 363-403, Doi 10.1029/94rg01872, 1994.

Li, H., Yang, Y., Hu, X.-M., Huang, Z., Wang, G., Zhang, B., and Zhang, T.: Evaluation of retrieval methods of daytime convective boundary layer height based on lidar data, Journal of Geophysical Research: Atmospheres, 122, 4578-4593, 10.1002/2016jd025620, 2017a.

Li, J., Li, C., Zhao, C., and Su, T.: Changes in surface aerosol extinction trends over China during 1980-2013 inferred from quality-controlled visibility data, Geophysical Research Letters, 43, 8713-8719, 10.1002/2016gl070201, 2016.

Li, T., Ban, C., Fang, X., Li, J., Wu, Z., Feng, W., Plane, J. M. C., Xiong, J., Marsh, D. R., Mills, M. J., and Dou, X.: Climatology of mesopause region nocturnal temperature, zonal wind and sodium density observed by sodium lidar over Hefei, China (32°N, 117°E), Atmospheric Chemistry and Physics, 18, 11683-11695, 10.5194/acp-18-11683-2018, 2018.

Li, Z., Guo, J., Ding, A., Liao, H., Liu, J., Sun, Y., Wang, T., Xue, H., Zhang, H., and Zhu, B.: Aerosol and boundary-layer interactions and impact on air quality, National Science Review, 4, 810-833, 10.1093/nsr/nwx117, 2017b.

Lux, O., Lemmerz, C., Weiler, F., Marksteiner, U., Witschas, B., Rahm, S., Schäfler, A., and Reitebuch, O.: Airborne wind lidar observations over the North Atlantic in 2016 for the pre-launch validation of the satellite mission Aeolus, Atmospheric Measurement Techniques, 11, 3297-3322, 10.5194/amt-11-3297-2018, 2018.

Manninen, A. J., Marke, T., Tuononen, M., and O'Connor, E. J.: Atmospheric Boundary Layer Classification With Doppler Lidar, J Geophys Res-Atmos, 123, 8172-8189, 10.1029/2017JD028169, 2018.

Mattis, I., Ansmann, A., Althausen, D., Jaenisch, V., Wandinger, U., Müller, D., Arshinov, Y. F., Bobrovnikov, S. M., and Serikov, I. B.: Relative-humidity profiling in the troposphere with a Raman lidar, Applied optics, 41, 6451, 10.1364/ao.41.006451, 2002.

Miao, Y., Liu, S., Guo, J., Huang, S., Yan, Y., and Lou, M.: Unraveling the relationships between boundary layer height and PM2.5 pollution in China based on four-year radiosonde measurements, Environmental pollution, 243, 1186-1195, 10.1016/j.envpol.2018.09.070, 2018.

Murray, E. R., and van der Laan, J. E.: Remote measurement of ethylene using a CO(2) differential-absorption lidar, Applied optics, 17, 814-817, 10.1364/AO.17.000814, 1978.

Petaja, T., Jarvi, L., Kerminen, V. M., Ding, A. J., Sun, J. N., Nie, W., Kujansuu, J., Virkkula, A., Yang, X. Q., Fu, C. B., Zilitinkevich, S., and Kulmala, M.: Enhanced air pollution via aerosol-boundary layer feedback in China, Scientific reports, 6, 6, 10.1038/srep18998, 2016.

Qiu, J., Xia, H., Shangguan, M., Dou, X., Li, M., Wang, C., Shang, X., Lin, S., and Liu, J.: Micro-pulse polarization lidar at 1.5 mum using a single superconducting nanowire single-photon detector, Optics letters, 42, 4454-4457, 10.1364/OL.42.004454, 2017.

Qiu, S., Tang, Y., Jia, M., Xue, X., Dou, X., Li, T., and Wang, Y.: A review of latitudinal characteristics of sporadic sodium layers, including new results from the Chinese Meridian Project, Earth-Science Reviews, 162, 83-106, 10.1016/j.earscirev.2016.07.004, 2016.

5  Reitebuch, O.: Wind Lidar for Atmospheric Research, in: Atmospheric Physics, edited by: Schumann, U., Research Topics in Aerospace, Springer, Berlin, Heidelberg, 487-507, 2012.

Renaut, D., Pourny, J. C., and Capitini, R.: Daytime Raman-lidar measurements of water vapor, Optics letters, 5, 233-235, 10.1364/ol.5.000233, 1980.

10  Seibert, P.: Review and intercomparison of operational methods for the determination of the mixing height, Atmospheric Environment, 34, 1001-1027, 10.1016/s1352-2310(99)00349-0, 2000.

Seidel, D. J., Ao, C. O., and Li, K.: Estimating climatological planetary boundary layer heights from radiosonde observations: Comparison of methods and uncertainty analysis, J Geophys Res-Atmos, 115, 10.1029/2009jd013680, 2010.

Seidel, D. J., Zhang, Y. H., Beljaars, A., Golaz, J. C., Jacobson, A. R., and Medeiros, B.: Climatology of the planetary boundary layer over the continental United States and Europe, J Geophys Res-Atmos, 117, 10.1029/2012jd018143, 2012.

15  Shang, X., Xia, H., Dou, X., Shangguan, M., Li, M., and Wang, C.: Adaptive inversion algorithm for 1.5 μm visibility lidar incorporating in situ Angstrom wavelength exponent, Optics Communications, 418, 129-134, 10.1016/j.optcom.2018.03.009, 2018.

Shangguan, M., Xia, H., Wang, C., Qiu, J., Lin, S., Dou, X., Zhang, Q., and Pan, J. W.: Dual-frequency Doppler lidar for wind detection with a superconducting nanowire single-photon detector, Optics letters, 42, 3541-3544, 10.1364/OL.42.003541, 2017.

20  She, C. Y., Yu, J. R., Latifi, H., and Bills, R. E.: High-spectral-resolution fluorescence light detection and ranging for mesospheric sodium temperature measurements, Applied optics, 31, 2095-2106, 10.1364/AO.31.002095, 1992.

Song, C., Wu, L., Xie, Y., He, J., Chen, X., Wang, T., Lin, Y., Jin, T., Wang, A., Liu, Y., Dai, Q., Liu, B., Wang, Y. N., and Mao, H.: Air pollution in China: Status and spatiotemporal variations, Environmental pollution, 227, 334-347, 10.1016/j.envpol.2017.04.075, 2017.

25  Stull, R. B.: An Introduction to Boundary Layer Meteorology, Kluwer Academic Publishers., Dordrecht. The Netherlands., 1988.

Su, T., Li, Z., and Kahn, R.: Relationships between the planetary boundary layer height and surface pollutants derived from lidar observations over China: regional pattern and influencing factors, Atmospheric Chemistry and Physics, 18, 15921-15935, 10.5194/acp-18-15921-2018, 2018.

Vogelezang, D. H. P., and Holtslag, A. A. M.: Evaluation and model impacts of alternative boundary-layer height formulations, Boundary-Layer Meteorology, 81, 245-269, 10.1007/bf02430331, 1996.

30

Wang, C., Xia, H., Shangguan, M., Wu, Y., Wang, L., Zhao, L., Qiu, J., and Zhang, R.: 1.5 μm polarization coherent lidar incorporating time-division multiplexing, Optics express, 25, 20663-20674, 10.1364/OE.25.020663, 2017.

Wei, W., Zhang, H., Wu, B., Huang, Y., Cai, X., Song, Y., and Li, J.: Intermittent turbulence contributes to vertical dispersion of PM$_{2.5}$ in the North China Plain: cases from Tianjin, Atmospheric Chemistry and Physics, 18, 12953-12967, 10.5194/acp-18-12953-2018, 2018.

35

Xia, H., Sun, D., Yang, Y., Shen, F., Dong, J., and Kobayashi, T.: Fabry-Perot interferometer based Mie Doppler lidar for low tropospheric wind observation, Applied optics, 46, 7120, 10.1364/ao.46.007120, 2007.

Xia, H., Dou, X., Sun, D., Shu, Z., Xue, X., Han, Y., Hu, D., Han, Y., and Cheng, T.: Mid-altitude wind measurements with mobile Rayleigh Doppler lidar incorporating system-level optical frequency control method, Optics express, 20, 15286-15300, 10.1364/OE.20.015286, 2012.

40

Xia, H., Dou, X., Shangguan, M., Zhao, R., Sun, D., Wang, C., Qiu, J., Shu, Z., Xue, X., Han, Y., and Han, Y.: Stratospheric temperature measurement with scanning Fabry-Perot interferometer for wind retrieval from mobile Rayleigh Doppler lidar, Optics express, 22, 21775-21789, 10.1364/OE.22.021775, 2014.

Xia, H., Shentu, G., Shangguan, M., Xia, X., Jia, X., Wang, C., Zhang, J., Pelc, J. S., Fejer, M. M., Zhang, Q., Dou, X., and Pan, J. W.: Long-range micro-pulse aerosol lidar at 1.5 μm with an upconversion single-photon detector, Optics letters, 40, 1579-1582, 10.1364/OL.40.001579, 2015.

45

Yang, T., Wang, Z., Zhang, W., Gbaguidi, A., Sugimoto, N., Wang, X., Matsui, I., and Sun, Y.: Technical note: Boundary layer height determination from lidar for improving air pollution episode modeling: development of new algorithm and evaluation, Atmospheric Chemistry and Physics, 17, 6215-6225, 10.5194/acp-17-6215-2017, 2017.

50  Zhang, Q., He, K., and Huo, H.: Policy: Cleaning China's air, Nature, 484, 161-162, 10.1038/484161a, 2012.

**Table 1. Key Parameters of the Integrated Lidar.**

| Parameter | CDL | DDL |
|---|---|---|
| Wavelength | 1548 nm | |
| Pulse Duration | 300 ns | |
| Pulse Energy | 110 μJ | |
| Repetition frequency | 10 kHz | |
| Diameter of collimator | 80 mm | |
| Diameter of telescope | 80 mm | 70 mm |
| Spatial resolution | 45 m | |
| Temporal resolution | 2 s | |
| Maximum range | 15 km | |
| Azimuth scanning range | 0 - 360 ° | |
| Zenith scanning range | 0 - 90 ° | |

**Table 2. The correlations between BLH and PM$_{2.5}$ and the inverse fitting results.**

| Time | Before precipitation | | | After precipitation | | |
|---|---|---|---|---|---|---|
| ABL category | CBL | CBL | RL | CBL | CBL | RL |
| BLH | BLH$_{RCS}$ | BLH$_{VAR}$ | BLH$_{RCS}$ | BLH$_{RCS}$ | BLH$_{VAR}$ | BLH$_{RCS}$ |
| C[a] | -0.92 | -0.89 | -0.93 | -0.34 | -0.21 | -0.22 |
| A[b] | 7.98 | 12.46 | 23.16 | | | |
| B[b] | 42.22 | 35.92 | 32.65 | | | |
| R$^{2}$ [c] | 0.84 | 0.65 | 0.85 | | | |

[a] C: Correlation coefficients.

[b] A/B: The parameters of the inverse fitting formula *PM$_{2.5}$=A+B/BLH*.

[c] R$^2$: Coefficient of determination of the inverse fitting.
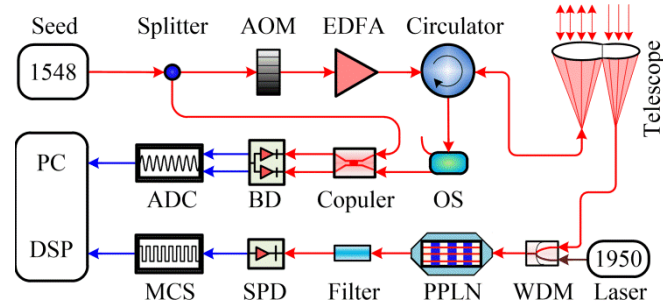
**Figure 1: The diagram of the integrated lidar system.**
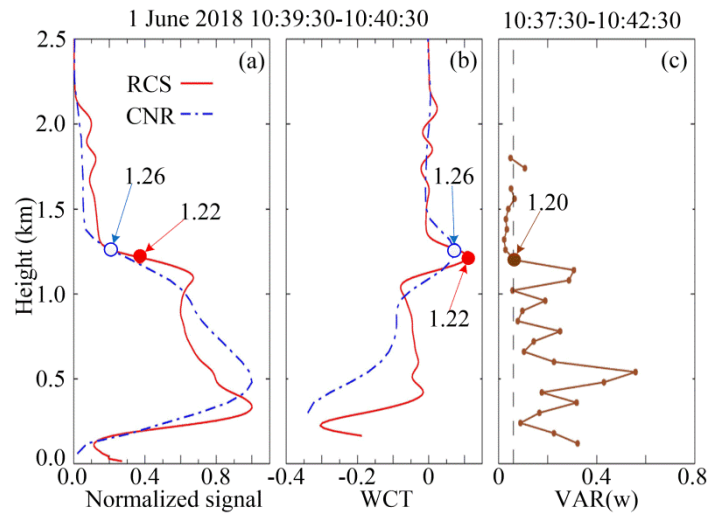
**Figure 2: (a) 1 min mean normalized RCS and CNR profiles. (b) The corresponding HWCT results of the RCS and CNR profiles in (a). (c) The vertical velocity variance profile. The black dashed line indicated the threshold of 0.06 m²s⁻². The red solid circle, blue circle and brown solid circle denoted by the arrows indicate the retrieved BLH, with the values at the end of the arrows.**
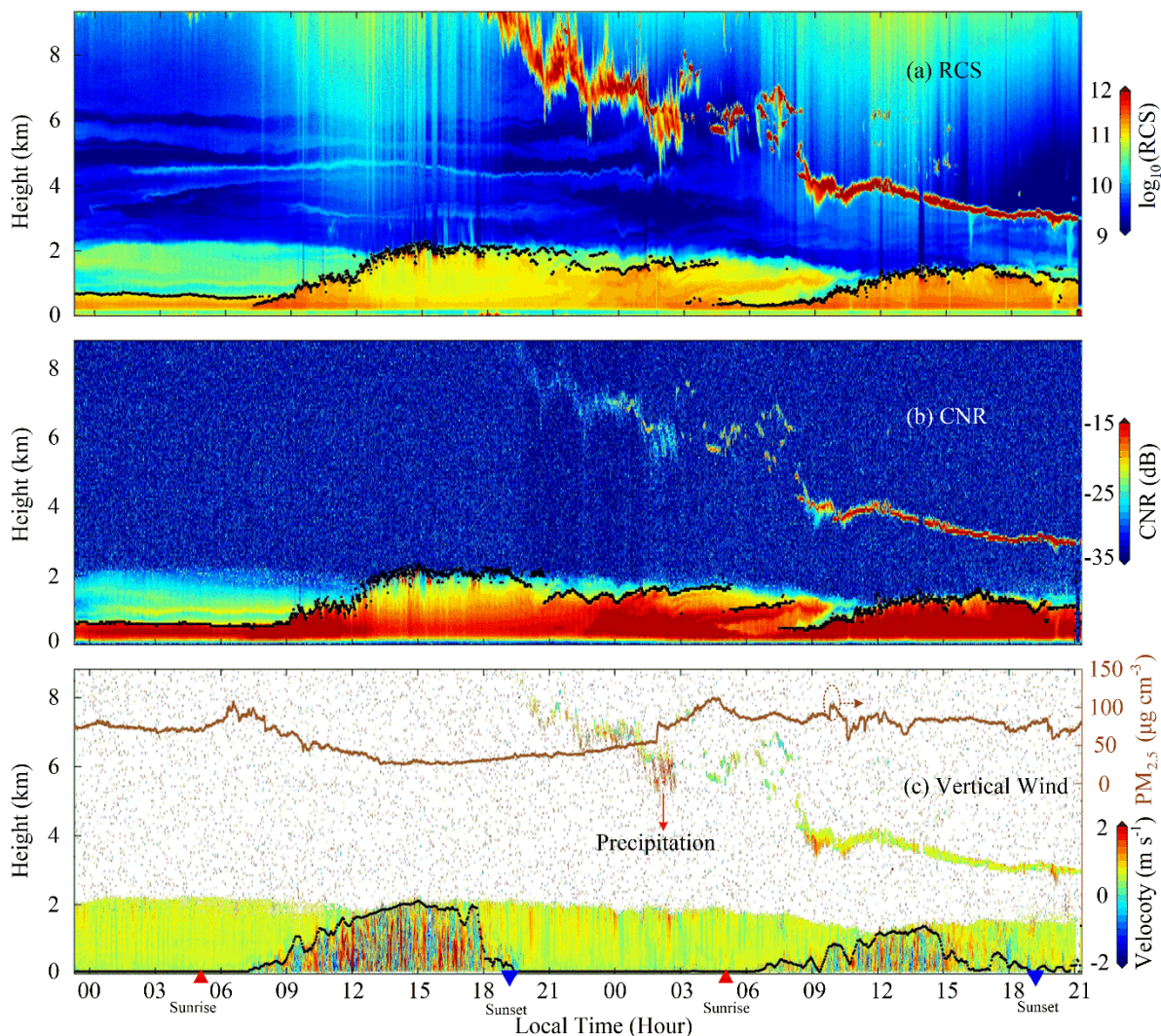
**Figure 3: Lidar observational results from 1 June 2018 to 2 June 2018. (a) The 1 min mean time series of logarithmic RCS profiles measured by DDL. The height time cross section of (b) CNR and (c) vertical wind measured by CDWL with 20 s temporal interval. The downward (upward) vertical wind is positive (negative). The brown dotted line indicates the PM$_{2.5}$ concentration near the ground. The black dotted lines in each panel indicates the BLH retrieved from RCS, CNR and vertical wind, respectively.**
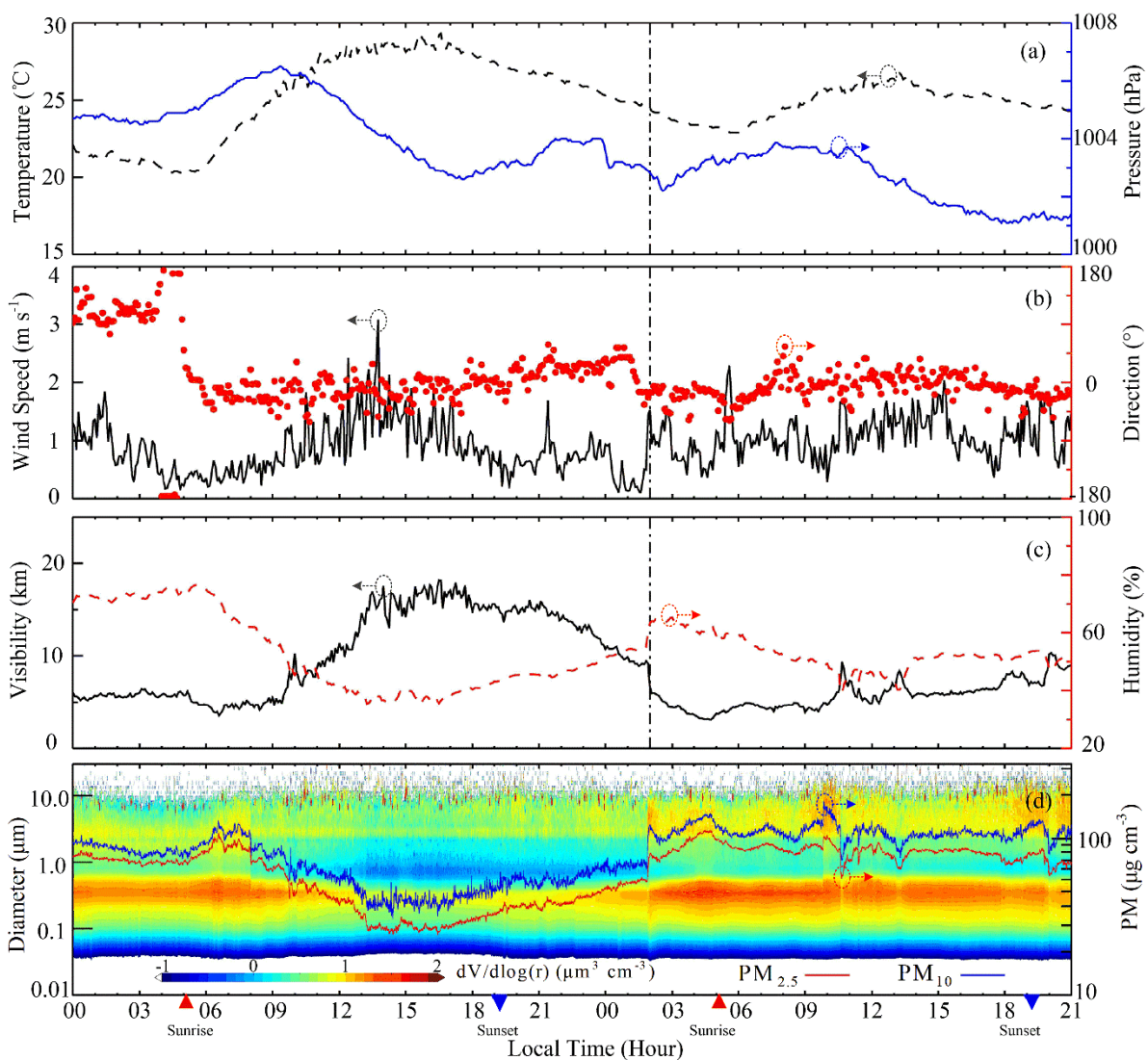
**Figure 4: The simultaneous measured surface meteorological parameters during the experiment from 1 June 2018 to 2 June 2018. From top panel to bottom panel are (a) temperature, pressure; (b) wind velocity, wind direction; (c) visibility, relative humidity; (d) logarithmic aerosol volume size, PM2.5 and PM10 concentration, respectively. The vertical dashed lines in (a)-(c) indicate the time when there is a sudden enhancement of PM2.5 in (d).**
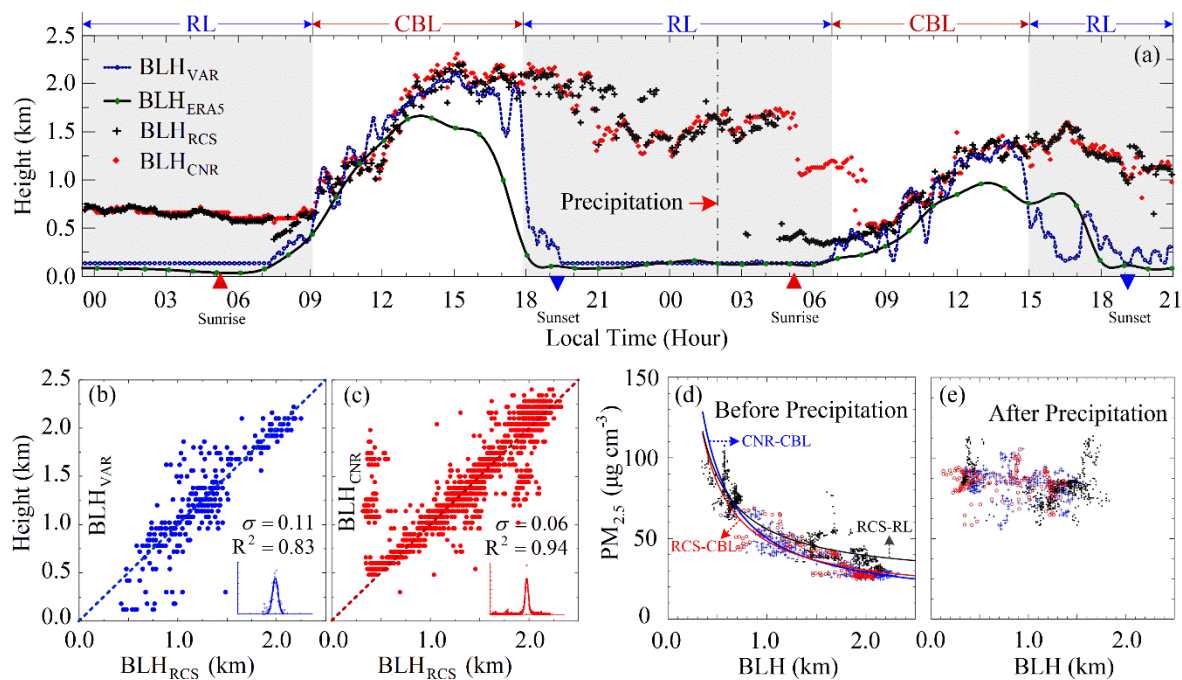
**Figure 5: (a) The BLH retrieval results from different methods. Scatter plots of (b) BLH$_{VAR}$ in CBL and (c) BLH$_{CNR}$ in CBL and RL versus BLH$_{RCS}$ for comparison. The blue and red dashed lines indicate x = y. The BLH differences are plotted in right bottom in (b) and (c). The blue and red solid lines represent the corresponding Gauss fitting. $R^2$ represents the coefficient of determination and σ represents the standard deviation of Gauss fitting. (d) The scatter plot of BLH and PM2.5 before precipitation. Red circles indicate BLH$_{VAR}$ in CBL, while blue pluses indicate BLH$_{RCS}$ in CBL and black dots indicate BLH$_{RCS}$ in RL. The solid lines represent the corresponding inverse fit. (e) Same as (d) but without inverse fitting after precipitation.**